Triaxial 3-D-Channeled Soft Optical Sensor for Tactile Robots

Matteo Lo Preti, *Associate Member, IEEE*, Federico Bernabei, *Graduate Student Member, IEEE*, Anderson B. Nardin, *Student Member, IEEE*, and Lucia Beccai, *Member, IEEE*

***Abstract*—Soft optical transducers have the potential to fulfill the need for advanced tactile sensing in robotics. We present a fingertip-shaped soft sensor with optically transparent channels that relies on soft materials and sensor morphology to measure an applied triaxial force. The proposed 3D-channeled sensor has a volume of 2.5 cm^3, and the experimental results reveal a 15-fold increase in voltage compared to its bulk analogous, showcasing a sensitivity of 0.34 and 0.09 N/mV to tangential and normal forces. A prototype with a diameter of 2 mm (0.4×) indicates the feasibility of scaling down the sensor. Force magnitude is estimated with a linear model and then decomposed into its F_{xy} and F_z with an R^2 of 0.93 and 0.98 within a sensing range of 4.05 and 8.50 N, respectively. A coordinate transformation from a covariant to a Cartesian reference frame is used to retrieve the direction of the tangential component of the force. The sensor was integrated into a compliant robotic hand as a proof-of-concept to demonstrate real-time operation in typical grasping tasks. The results of this work show new possibilities for scalable optical soft sensors to provide complete local information about the interaction forces in soft/rigid robots.**

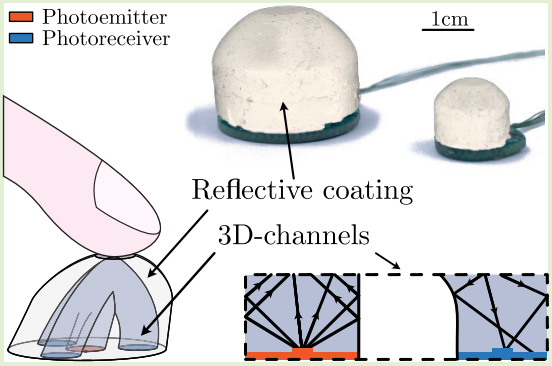

***Index Terms*— Force and tactile sensing, perception for grasping and manipulation, soft robot materials and design.**

I. Introduction

TACTILE sensing enables robots to interact with the physical world and perform dexterous tasks [1]. Soft optical sensors are making an impact as an enabling technology in soft robotics [2]. They rely on soft materials to modulate light properties upon mechanical deformations [3]. Despite offering several advantages, research is less prolific than that on other transduction principles, e.g., capacitive [4], [5] and resistive [6], [7]. For example, optical sensors have intrinsic immunity from electromagnetic interference [8] and do not require electrically conductive materials, which usually limit the mechanical robustness of the transducer that deforms both by externally applied forces and by the inherent passive or active deformation of a soft robot [9].

Triaxial soft sensors pose significant developmental challenges, with a few examples in recent years [10], [11]. In 2018, Dwivedi et al. [12] designed, modeled, and validated a soft magnetic triaxial force sensor. It comprises a pyramid-shaped tactile unit with a three-axis Hall element and one magnet embedded in a silicone rubber substrate. In the following year, Kawasetsu et al. [13] presented a flexible and soft inductive three-axis tactile sensor that incorporated flexible inductive coils and a liquid metal as a target layer to address the sensitivity-softness tradeoff typical of this transduction method. However, environmental factors (e.g., magnetic fields) and mechanical fatigue compromise the stability and reliability of these solutions. In 2021, Gong et al. [14] introduced a flexible tactile sensor array for dynamic triaxial force measurement based on aligned piezoresistive nanofibers. The sensor comprises a flexible substrate, piezoresistive layer, and conductive layer. The conductive layer is patterned into a serpentine shape to reduce the effect of bending on resistance changes. Nevertheless, piezoelectric materials exhibit nonlinear behavior, which affects the measurement range, linearity, hysteresis, and sensor drift. Examples of triaxial optical sensors are also limited and mainly rely on fiber Bragg grating (FBG). In 2018, Gao et al. [15] proposed an FBG-based triaxial force

Manuscript received 19 June 2024; accepted 6 July 2024. Date of publication 16 July 2024; date of current version 1 September 2024. This work was supported by the European Union's Horizon 2020 Program under Grant 863212 PROBOSCIS. The associate editor coordinating the review of this article and approving it for publication was Dr. Wei Wei. *(Corresponding authors: Matteo Lo Preti; Lucia Beccai.)*

Matteo Lo Preti and Lucia Beccai are with the Istituto Italiano di Tecnologia, 16163 Genoa, Italy (e-mail: matteo.lopreti@iit.it; lucia.beccai@iit.it).

Federico Bernabei and Anderson B. Nardin are with the Istituto Italiano di Tecnologia, 16163 Genoa, Italy, and also with The BioRobotics Institute, Scuola Superiore Sant'Anna, 56025 Pontedera, Italy (e-mail: federico.bernabei@iit.it; anderson.nardin@iit.it).

This article has supplementary downloadable material available at https://doi.org/10.1109/JSEN.2024.3425835, provided by the authors.

Digital Object Identifier 10.1109/JSEN.2024.3425835

sensor with parallel flexure hinges to sense the contact force within a range of ±0.98 N on the xy plane and 0–0.95 on the z-axis. However, optical fibers may decrease durability and robustness, and data can be affected by external light sources and temperature changes. Two years later, Li et al. [16] developed a high-resolution triaxial catheter tip force sensor with miniature flexure and suspended optical fibers for thermal compensation. The flexure, consists of a thin metal sheet, is designed to be compliant in the axial direction but stiff in the radial direction. This solution can be used to measure force within a range of ±0.8 N on the xy plane and from 0 to 0.8 N on the z-axis. In the following year, Deng et al. [17] presented a miniature triaxial fiber-optic force sensor for flexible ureteroscopy, consisting of an FBG attached to the inner surface of a cylindrical shell. The shell is made of a transparent material and eccentrically configured with respect to the FBG. When a force is applied to the shell, the strain is induced in the FBG, causing a shift in the Bragg wavelength. The measurement range of this solution is ±2 N on the xy plane and from 0 to 4 N on the z-axis. However, crosstalk between fibers may alter the signal and lower the resolution and accuracy, and the presence of triaxial fibers requires complex mathematical modeling and calibration. Cao et al. [18] developed a polymer-based optical waveguide triaxial tactile sensor for 3-D curved shells in 2022. The measurement range of this solution is ±1 N on the xy plane and from 0.1 to 1 N on the z-axis. Although this sensor can be easily fabricated via 3-D printing and UV curing, the requirement of a bulky line scan camera strongly limits its integrability. One year later, Li et al. [19] presented an optical-waveguide-based triaxial tactile sensor for laparoscopic applications using the light intensity of three intersecting planar channels to measure forces from 0 to 3 N, at the cost of expensive demodulation equipment and complex internal wiring.

In addition to academic research, noteworthy commercial solutions include OptoForce and GelSight. OptoForce uses photoreceivers (PRs) to measure the amount of reflected light emitted by a photoemitter (PE) within its bulk structure [20], [21]. The force vector can be reconstructed by comparing the measured values of each PR. However, the 5–7.5-mm-thick rigid base of this sensor may compromise its integrability into nonrigid platforms. Indeed, the sensor response may be affected by the full range of motions and deformations of soft robotic systems, and it is primarily designed for rigid robots and linear or rotational movements. On the other hand, GelSight is a tactile sensing technology that employs a block of transparent rubber coated with metallic paint to conform to the shape of an object and provide a detailed 3-D map of its surface. The sensor comprises a flexible substrate, a piezoresistive layer, and a conductive layer. Although GelSight sensors are primarily designed to provide high-resolution surface topography measurements, recent research has focused on enhancing their three-axis force sensing capability. For example, L3 F-TOUCH [22] is a wireless GelSight sensor with decoupled tactile and three-axis force sensing within a force range of ±2 N in the xy plane and 12 N in the z-axis.

Despite recent advancements in soft sensors, their applicability in tactile robotics remains challenging [23], [24], [25], [26]. Optical sensors provide inherently robust measurements. However, only recently, research has started to go beyond FBG-based solutions [27]. Given the proven potential of optical sensing, we think that new designs for soft optical transducers are needed, overreaching the basic structures developed so far, which can exploit morphology and soft materials to detect triaxial force [28], and that do not rely on bulky electronics. This way, seamless integration into a broad spectrum of intelligent robotic systems could be addressed.

This article introduces the design and characterization of a triaxial soft optical waveguide sensor based on a 3-D-channeled architecture and its demonstration when integrated into a custom-compliant robotic hand. The proposed solution aims at: 1) triaxial force reconstruction using soft materials; 2) size and sensing range that can be tailored to meet application-related requirements; and 3) the potential for seamless integration in both rigid and deformable systems without the need for a bulky transduction system. Taking into account these objectives, the challenge faced in this work consisted of creating a compact triaxial soft optical sensor based on a cost-effective fabrication process and materials.

Section II-A describes the design of the proposed sensor. The fabrication procedure is then detailed in Section II-B. Section II-C presents the characterization methodology and process. Finally, the integration of a real-time prototype in a robotic hand is demonstrated in Section II-D. Section III shows the results and discusses them, and Section IV reports conclusive remarks.

II. Methods

The 3-D-channeled soft optical sensor illustrated in Fig. 1 consists of a soft hemispherical structure with a central PE and three PRs radially distributed at 120° at its base. Light is transmitted through optically clear channels from the PE to the PRs. An absorbing spot resides within the sensor opposite to the PE, and the entire structure is embedded in a reflective material. In the absence of an external force [Fig. 1(a)], light propagates isotropically in the channels. When a normal force is applied [Fig. 1(b)], the absorbed light increases and reaches the PRs in an equal manner. By contrast, a tangential force displaces the black spot along the force vector, inducing anisotropies in the light pathway. In this case, shown in Fig. 1(c), the light in the channel aligned with the force direction is further reduced, whereas that in the opposite direction increases.

This concept is investigated and compared with a bulk analog (without optical channels) and a 0.4 × scaled-down version.

A. Sensor Design and FEM Simulations

The internal structure of the sensor was simulated using the Solid Mechanics and Geometrical Optics toolboxes of COMSOL Multiphysics[1] (COMSOL Inc., Sweden). The base of the sensor was modeled as a central conical light source instead of the light emitter and three sinks spaced at 120°. Three geometries were compared: the first one with a base radius of 8.5 mm and a height of 12.5 mm, with channels of ∅ = 4.4 mm at 5.5 mm from the center; the second one with

[1]Registered trademark.

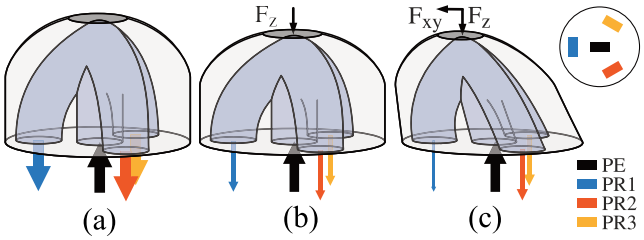

Fig. 1. Concept of the 3-D-channeled sensor with a central PE and radially placed PRs, as sketched in the top-right base cross section. (a) In the resting state, light is partially absorbed and partially reflected evenly in the channels. (b) Upon application of a normal force, more light is absorbed than transmitted to the PRs. (c) When the force has a nonnull tangential component $\vec{F}_{xy}$, more light is absorbed in the channel aligned with $\hat{F}_{xy}$, and less in the opposite direction.

a base radius of 3.9 mm and a height of 5.7 mm and channels $\varnothing = 2$ mm at 2.5 mm from the center (a scaled-down version of the first geometry by a factor 0.4); and the third bulk one with a base radius of 8.5 mm and a height of 12.5 mm without channels with a wall thickness of 0.8 mm (comprised in the provided dimensions, such that its size matches with the first geometry). Variations in the channels and bulk geometries are shown on the left side of Fig. 2(a). The material of the channels/inner structure is polydimethylsiloxane (PDMS) with a refractive index of 1.42. In contrast, the external dome embedding the channels is modeled as a modified PDMS with matched Young's modulus and a refractive index of 1 to ensure total internal refraction. In all scenarios, a displacement was prescribed at the top of the sensor. The force components along the three axes were used to verify whether the PRs could measure relative differences proportional to the resulting load. The number of rays arriving at the sensor wall change based on sensor geometry and displacement. Fig. 2(b) shows these values as RGB channels of an image while varying x, y, and z. The number of rays is presented in Fig. S1, keeping the channels separate. The corresponding image in the hue-saturation-value (HSV) space is reported in Fig. S2. Color changes indicate a variation in the relative value of the three sinks, whereas saturation changes indicate that all three values changed. These alterations occur when the tangential and normal force vary, respectively. The 3-D-channeled geometry received 20 × more rays than the bulk version, thus corroborating the choice of building a channeled light path. Although the bulk solution can theoretically work, it requires signal amplification and has a lower signal-to-noise ratio. Despite comparable variations between the 2- and 4.4-mm channels, the changes were smoother and more consistent in the larger version, with larger responses to normal loads.

We further investigated the relationship between the sensor's stiffness and conveyed rays by simulating the 4.4-mm channels geometry within a Young's modulus from 0.56 to 3.59 kPa. This range includes the commonly used variability in PDMS casting [29]. As reported in Fig. S3, the normalized fraction of rays arriving at the walls decreases with an applied normal force up to 3 N, with an increase in rays intensity of 4.76 × using a 30:1 mix ratio with respect to a 5:1.

B. Fabrication and Electronics Development

The sensor manufacturing process is described in Fig. 3(a). The molds were designed using SolidWorks (Dassault Systems

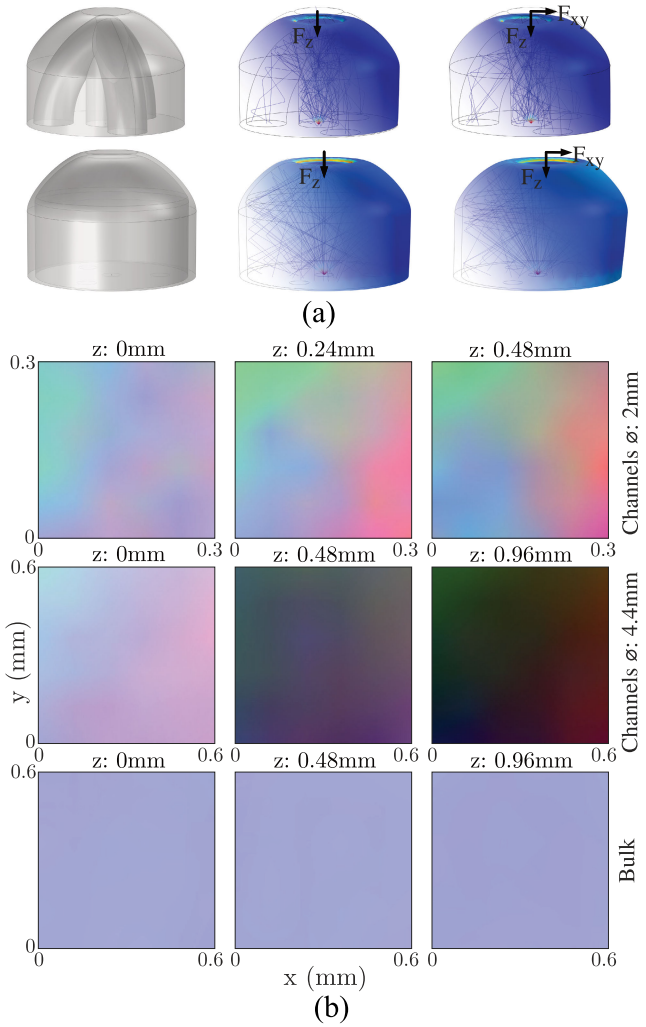

Fig. 2. Finite element model (FEM) simulations of the three compared designs: $\varnothing_{Ch}$ = Bulk, 2 and 4.4 mm. (a) Geometries chosen for the simulation with channels $\varnothing = 2$ and 4.4 mm (the second is shown for visualization purposes), and without channels. The unloaded structures are sketched, and the stresses upon perpendicular and axial loads are shown together with the rays' distribution. (b) Activation level of the three PRs shown as RGB channels when varying X, Y, and Z of the applied displacement on the sensor. Different patterns for different tactile locations can be identified in the three tested scenarios. Color changes indicate a variation in the relative values at each sensor wall, whereas changes in saturation indicate the x, y, and z values are all changing for a specific sensor.

SolidWorks Corporation, MA, USA) and 3-D-printed. The molds for the channels are made in Model Resin v3 (Formlabs Inc., MA, USA) with an stereolithography (SLA) printer, while the remaining parts are made in acrylonitrile butadiene styrene (ABS) with an Ultimaker S3 (Ultimaker B.V., The Netherlands) fused deposition modeling (FDM) printer. The selection of the manufacturing process and materials was deliberate, aiming at enhancing the optical characteristics of the sensor and improving the deformation, thus the sensor response. All structural layers were cast using PDMS (Sylgard 184, Dow Inc., MI, USA) at a 30:1 mix ratio. While the internal channels comprised pure PDMS, the upper spot incorporated a 3% mixture of black ink (Silc Pig, Smooth-On, Inc., PA, USA), and the outer shell featured a blend of 4.3% titanium dioxide particles (TiO_2) to match the mechanical

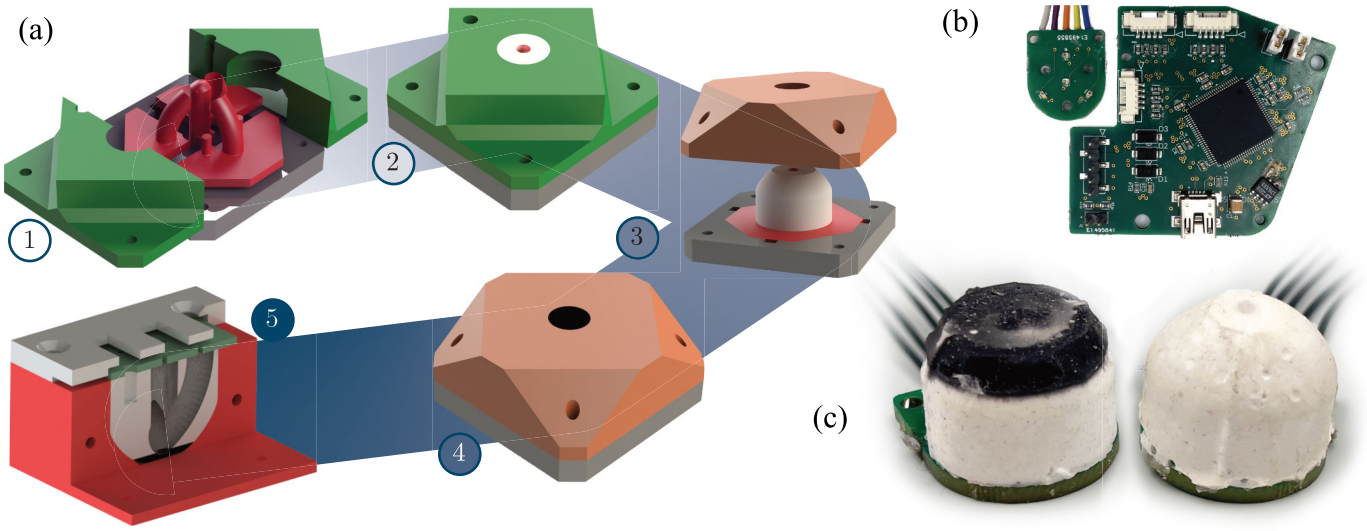

Fig. 3. Sensor fabrication procedure and prototypes. (a) Visual representation of the steps to fabricate the prototypes with embedded channels for the external shell (1) and (2), black spot (3) and (4), and internal channels (5). (b) Sensor substrate and preprocessing boards. (c) Images of the cast prototypes with and without channels (left and right, respectively).

and chemical properties of the core, and ensure shielding from external light disturbances [30]. Each formulation was mixed for 30 s using a Thinky ARE-250 mixing and degassing machine (THINKY USA, INC, Laguna Hills, CA, USA), followed by an additional degassing step of 5 min using the S-26P-NL vacuum degassing system (Easy Composites EU BV, Rijen, The Netherlands). As shown in Fig. 3(a)(1) and (2), the outer shielding layer was obtained using a seven-piece mold. The inner one (in red) creates the internal space for the channels, whereas the external one (in green) defines the cladding volume. Once the material was poured inside, curing was completed by placing the part in an oven at 60 °C for 3 h. The black spot was fabricated using an analogous approach by substituting the top section of the mold, as shown in Fig. 3(a)(3) and (4). Ultimately, uncured PDMS is injected into the empty cavities provided by the red parts in (1), aligning the printed circuit board and completing the curing process in an oven at 60 °C for 3 h, as shown in Fig. 3(a)(5). The bulk prototype was fabricated using the procedure schematized in Fig. S4. The outer shell was cast (1) and then inserted into a second mold (2), in which the black spot and PDMS were poured and cured in sequence. The two prototypes of the same size are shown in Fig. 3(c). A black coating on top of the channeled prototype was used to distinguish it from the bulk one without affecting the sensor response. As shown in Fig. 3(a), although the manufacturing process was designed to minimize the number of steps and thereby reduce variability dependent on the manufacturer's skill, the complexity of the structure and the small size of the channels precluded the possibility of subjecting the uncured sample to a degassing process at all stages. This limitation resulted in a rough external surface finish. Notably, these surface irregularities are confined to the external surface in both cases and in the order of magnitude of the mold resolution. From a functional perspective, it is pertinent to consider whether these surface irregularities impact performance. However, given the thicknesses of the PDMS + TiO_2 layer in both cases, particularly in the channeled prototype and the size of the irregularities, it is reasonable to conclude that they are unlikely to have any significant effect on signal variation in response to the applied force. The sensor requires one central near-infrared PE (KP-1608F3C) and three matched PRs (KP-1608P1C) positioned at 120° from the center. As shown in Fig. 3(b), a board was used as the sensor substrate, and a custom external board was developed to drive three sensors.

The 50 × 60 mm preprocessing board hosts surface-mount device (SMD) resistors (84 Ω for the PE and 18 KΩ for the PRs) and a programmable system-on-chip (PSoC) (Cypress CY8C5667AXI-LP040, Infineon Technologies) to preprocess and digitalize raw data from up to three connected sensors. An analog multiplexer sequencer was placed in cascade with a programmable gain amplifier ($G = 16$) and a 12-bit analog to digital converter (ADC) successive-approximation register (SAR). The output signal containing the values of nine PRs is streamed by averaging 74 samples for each PR using either the inter-integrated circuit (I2C) protocol or microUSB at 100 Hz.

C. Testing and Characterization

The sensor was characterized using the experimental setup shown in Fig. S5. Two orthogonal servo-controlled linear stages (M-126-GC1, PI, Karlsruhe, Germany) are at the base of the setup, with a custom housing for the sample to be tasted. Three orthogonal manual micrometric translation stages (M-105.10, PI) were used to manually adjust the micrometric servo-controlled translation stage (M-111.1DG, PI). A displacement along the three axes was applied to the sensor and measured through a triaxial load cell (ATI Nano 17, ATI Industrial Automation, Inc.) interfaced with an ABS probe brought into complete contact with each cell surface. Force data were captured using a DAQ (USB-6218, NI), whereas sensor data were acquired from the preprocessing board with serial communication to a host computer at 50 Hz. A custom LabVIEW interface ensured communication with instrumentation, data synchronization, and logging. The protocol for the acquisitions

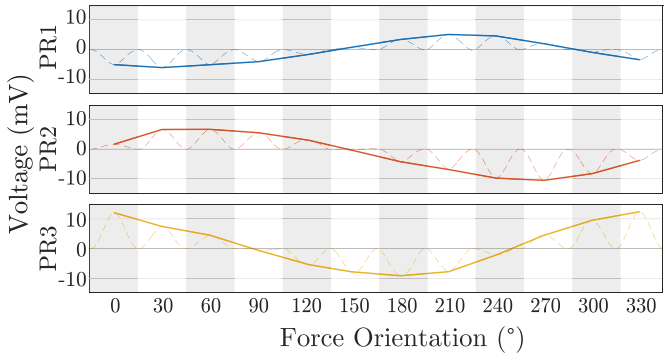

Fig. 4. Average cycle of the three PRs when $z = 2$ mm. The maximum values are connected to show the phase shift of 120° among them.

initializes the communication with the hardware peripherals and brings the motor to the highest vertical position. The vertical and horizontal positions are controlled via software, so each acquisition starts at the same probe–sensor distance. For eight indentation depths (0.25–2 mm), the sample was moved along a given direction on the xy plane up to 1 mm for ten cycles. The test was repeated in the xy plane from 0° to 345° at intervals of 15°. Another test was carried out by indenting the sensor for 11 trials up to 2 mm along the z-axis. All tests were performed with a motor speed of 0.1 mm/s.

Data were processed using MATLAB (The MathWorks, Inc.). To identify the best processing workflow, the relative change in the three PRs with the direction of the force applied on the xy plane was investigated, considering their spatial relationship. Fig. 4 shows the maximum value of the average cycle at $z = 2$ mm for each PR while varying the direction of F_{xy}. The relative voltage phase shift reflects the 120° spacing of the channels. A more detailed representation of the average curve for each PR is presented in Fig. S6, where their average curves are shown for each indentation level and 24 tested xy-directions.

The value of each PR was considered a component of one axis of a covariant reference frame. The magnitude of the resulting force and its planar orientation were obtained by a coordinate transformation from the covariant (r, t) to a Cartesian orthogonal (x, y) reference frame, as sketched in Fig. S7. The redundant configurations of the three PRs were exploited by considering the ordered tuples (PR_3 PR_2), (PR_2 PR_1), and (PR_1 PR_3) as components of the two axes spaced by an angle $\widehat{rt} = \vartheta = -2\pi/3$. The angle γ between r and x depends on for the three tuples as follows:

$$\gamma = 7\pi/6 - 2\pi/3(0 \quad 1 \quad 2) = (7\pi/6 \quad \pi/2 \quad -\pi/6). \tag{1}$$

The coordinates of a point $P = (r_P, t_P)$ in the covariant reference frame can be expressed as (x_P, y_P) in the Cartesian reference frame using the following transformation:

$$\begin{pmatrix} x_P \\ y_P \end{pmatrix} = M \cdot \begin{pmatrix} r_P \\ t_P \end{pmatrix} \tag{2}$$

where the rotational matrix M is defined as

$$M = \frac{1}{\sin(\theta)} \begin{bmatrix} \sin(\gamma + \theta) & -\sin(\gamma) \\ -\cos(\gamma + \theta) & \cos(\gamma) \end{bmatrix}. \tag{3}$$

The process is repeated for the three tuples to obtain $\mathbf{x}_P$ and $\mathbf{y}_P$. The angle α and magnitude ρ are then obtained by the Cartesian-to-polar transformation of the averages of the three estimations $\bar{\mathbf{x}}_P$ and $\bar{\mathbf{y}}_P$

$$\begin{cases} \alpha = \arctan \bar{\mathbf{x}}_P / \bar{\mathbf{y}}_P \\ \rho = \sqrt{\bar{\mathbf{x}}_P^2 + \bar{\mathbf{y}}_P^2}. \end{cases} \tag{4}$$

Once the direction of the force on the xy plane was obtained, its magnitude was calculated by considering the following decomposition:

$$\vec{F} = \vec{F}_{xy} + \vec{F}_z = F \cos\varphi \cdot \hat{r} + F \sin\varphi \cdot \hat{z} \tag{5}$$

with $\varphi \in [0, \pi/2]$. Given the normalized values of the three PRs $\mathrm{PR} = (\mathrm{PR}_1, \mathrm{PR}_2, \mathrm{PR}_3)$

$$\varphi = \frac{1}{2} \arctan\left(\frac{1}{2} \frac{\overline{\mathrm{PR}}}{1 + \sigma_{\mathrm{PR}}} - \overline{\mathrm{PR}} \right) + \frac{\pi}{4}. \tag{6}$$

A linear model is then used to fit the force F as

$$F = 0.1511 + \mathbf{PR} \cdot (0.1648 \quad 0.0446 \quad -0.0016). \tag{7}$$

Finally, the two components are calculated as

$$\begin{cases} F_{xy} = F \cdot \cos(\varphi) \\ F_z = F \cdot \sin(\varphi). \end{cases} \tag{8}$$

D. Sensor Integration

Three sensors were integrated into a compliant, underactuated robotic hand to evaluate their real-time operation. The hand is tendon-driven and controlled by three servomotors at its base, with five fingers that have different actuation mechanisms. The thumb and index finger are actuated individually, while the remaining fingers share a common tendon. Furthermore, sensor integration was selectively applied to the thumb, index, and middle fingers, whereas the ring and little fingers were equipped with passive PDMS fingertips.

Each finger has three phalanges interspersed with elastic hinges, except for the thumb, which has two phalanges and two hinges. Tension applied to the tendon induces concurrent closure of the finger hinges, resulting in flexion of the finger until complete closure or contact. The palm, back of the hand, and motor interfaces are made of ABS and tough polylactic acid (PLA), while the fingers are 3-D-printed using thermoplastic polyurethane (TPU). This material choice ensures the fingers can withstand repeated deformation and stresses incurred during bending.

The sensors were integrated into the distal phalanx of the fingers, tailored to accommodate their dimensions, with the sensor protruding 2 mm from the tip surface. The sensor's connection to the preprocessing board, housed at the back of the hand, was guided through an internal channel. Importantly, this connection did not interfere with the tendon housed in the adjacent blue channel.

The initialization phase sets up serial communication, user datagram protocol (UDP) sockets, dynamixel motors (XM430-W210, Robotis), and the proportional–integral–differential (PID) controller. The initial position is set as the slightest activation of the motors that causes a noticeable variation

in the bending of the fingers. During runtime, the algorithm monitors external commands through a UDP socket. In `open` mode, the hand is immediately reset to its initial position to ensure a reliable safety measure. In `catch` mode, $\bar{F}_z$ obtained from the sensors is monitored to detect contact while the hand gradually closes the fingers. When $\bar{F}_z > 0.6$ N, an object has been grasped. The pseudocode for the controller of the sensorized robotic hand is presented in Algorithm 1 in Supplementary Information.

While grasping a target, the algorithm observes $\mathbf{F}_{xy}$ and $\boldsymbol{\alpha}$. Certain angles represent forces associated with the object's slippage, whereas others are interpreted by the hand as an intentional attempt by a human user to take the object. The robotic hand smoothly opens its fingers if $20° < \alpha_{\text{thumb}} < 30°$ or $150° < \alpha_{\text{index}} < 160°$. These angles are defined by assuming a perpendicular orientation of the fingers to the ground plane. Angles out of such defined ranges indicate undesired movements of the object. In this way, the PID controller adequately modulates the pulling of the tendons and, consequently, the grasping force.

The entire system was mounted on a UR5e robotic arm (Universal Robots, Denmark) to validate the grasping performance of the sensorized hand during the grasp-and-lift [31] task.

III. Results and Discussion

Data from the prototypes with a base radius of 8.5 mm are shown in Fig. 5(a). Despite the lower response up to 4 mV, the bulk prototype exhibits observable coherent variations with the indentation depth. Although this simplified version can be used as a pressure sensor, changes in the signals induced by F_{xy} were not large enough for a reliable triaxial force reconstruction. In accordance with Fig. 2, the presence of channels gives a preferential traveling direction to the light. Consequently, the measured voltage increased by a factor of 15 with respect to that of the bulk prototype. Furthermore, the signal has a clearly distinguishable variability to normal and transversal forces with repeatabilities of (0.131 ± 0.044), (0.116 ± 0.033), and (0.136 ± 0.086) mV for the three signals.

The influence of channel size was investigated by fabricating a sensor with scaled-down dimensions ($\varnothing = 2$ mm). The two sensors were tested at indentation depths from 0.1 to 1 mm, up to 0.5 mm along the x- and y-directions for ten cycles. The ratio between the voltages of the two prototypes Ω_{PR} is shown in Fig. 5(b) for the three PRs. The voltage in the $\varnothing =$ 4.4-mm prototype is consistently larger than in the $\varnothing = 2$ mm one. For indentations $\gtrapprox$0.5 mm, the median value is constant, meaning that the two prototypes have coherent variations with F_z. The error bar represents the ratio between the measured signal variability and the transversal component at a given indentation depth. Lower values mean that the two sensors have comparable behaviors, whereas higher errors mean that the $\varnothing = 4.4$-mm prototype has greater voltage changes with F_{xy}. For each PRs, we have: $\overline{\Omega}_{\text{PR}_1} = 17.02 \pm 2.45$ on the x-axis and 16.86 ± 2.26 on the y-axis; $\overline{\Omega}_{\text{PR}_2} = 10.94 \pm 11.85$ on the x-axis and 11.06 ± 8.97 on the y-axis; and $\overline{\Omega}_{\text{PR}_3} = 10.66 \pm 4.08$ on the x-axis and 10.98 ± 3.55 on the y-axis. The precision in the fabrication

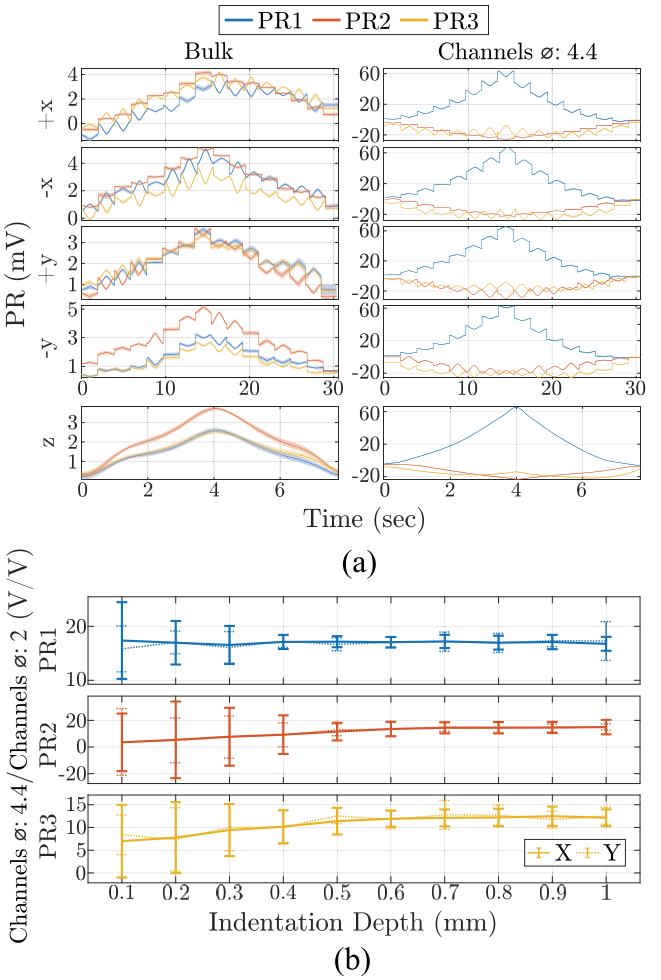

Fig. 5. Comparison of the signals of the prototypes. (a) Indentation and translational mechanical tests of the prototypes with the radius of 8.5 mm (bulk and channeled). (b) Voltage ratio of the three PRs in the prototypes with channels $\varnothing = 2$ and 4.4 mm.

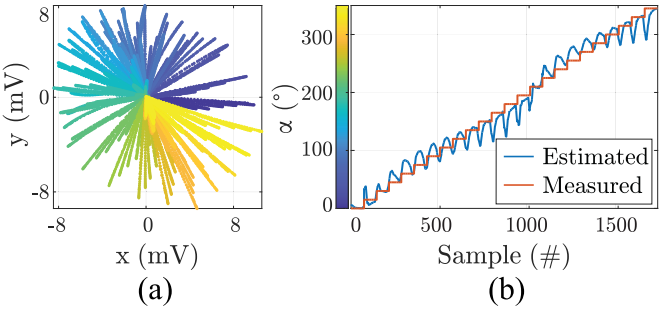

Fig. 6. Estimation of F_{xy}-direction. (a) Angular direction α in the Cartesian reference frame. (b) Estimated and measured force direction on the xy plane.

procedure of the scaled-down version may influence its behavior, especially at indentation depths lower than 0.5 mm. Moreover, a low yield of the fabrication process was observed given the low repeatability of PDMS curing within small channels. Nevertheless, as shown in the simulations and reflected in this test, the scaling process is feasible.

Fig. 6(a) shows the effect of the transformation from the covariant to the Cartesian reference frame [see (2)]. The

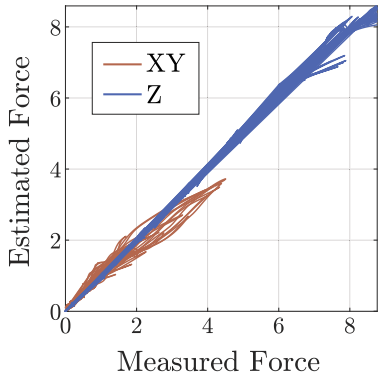

Fig. 7. Magnitude of the *xy* and *z* components of the force.

TABLE I
SUMMARY OF THE CHARACTERISTICS OF THE SENSOR

	XY	Z
FSO (N)	4.05	8.50
Sensitivity (mV/N)	0.20	11.02
Hysteresis (%)	13.94	6.62
R^2 (#)	0.93	0.98
MDF (mN)	140	3

color bar reflects the angle associated with data projected in the (x, y) reference frame. An actual comparison between the outcome of (4) and the reference angle is shown in Fig. 6(b), with a resulting mean squared error of 16.33°. The fluctuation is the error in the geometrical reconstruction, which increases with F_{xy}. Hence, it can be ruled out that internal deformations of the channels distort the physical "axes," i.e., the channels of the sensor, and can impact the triangulation accuracy. However, for practical use cases, this error does not compromise the applicability of the sensor. Indeed, shear force values registered during grasping experiments rarely exceeded 1 N, which is far below the full-scale output (FSO) value for $F_{xy} = 4.05$ N.

For F_z, the FSO is 8.50 N within the tested indentation range even though saturation was not reached. Fig. 7 shows the force estimated from (8) compared with the measured force values, with an R^2 of 0.93 and 0.98, a sensitivity of 0.20 and 11.02 mV/N, a minimum detectable force (MDF) of 140 and 3 mN, and a hysteresis of 13.94% and 6.62% for the xy and z components, respectively. A characterization summary is presented in Table I.

Differently from other solutions relying on the contact location to approximate tangential forces, like the Shokac Cube (Touchence Inc.), the proposed sensor detects force in the three axes from a single contact point at the tip. This solution is compared with the state-of-the-art soft optical sensors in Table II, from which it can be concluded that the present sensor achieves a remarkable range in the xy plane and a very good force value in compression. Moreover, despite being harder to compare directly, the achieved sensitivities lead to an MDF that is low enough for a broad application range.

Considering the integrated solution proposed by Yoshikai et al. [32], the PR is opposite to the PE. In contrast, all the elements can be positioned on the same side in the present channeled structure, allowing the sensor to interface

TABLE II
COMPARISON BETWEEN THE 3-D-CHANNELED OPTICAL SENSOR AND THE STATE-OF-THE-ART SOFT OPTICAL SENSORS

Group	F_{XY} (N)	F_Z (N)	s_{XY}	s_Z
Our Solution	±4.05	8.50	0.20 mV/N	11.02 mV/N
Gao et al. [15]	±0.98	0.95	NA	NA
Li et al. [16]	±0.8	0.8	1238 pm/N	376 pm/N
Deng et al. [17]	±2	4	95 pm/N	94 pm/N
Cao et al. [18]	±1	1	$-0.20\,\mathrm{N}^{-1}$	$-0.22\,\mathrm{N}^{-1}$
Li et al. [19]	±3	3	NA	NA
Li et al. [22]	±2	12	0.07 N/pixel	0.32 N/pixel

with the outside world without any components at the interface that could impair compliance at contact. Moreover, using polyurethane foam on top of the cited sensor hugely dumps the performance and temporal resolution of the same, which is more likely to act as an on/off, rather than a dynamic sensor.

The sensor was integrated into a rigid case to assess its real-time response to dynamic and static loads. Video S1 shows the sensor's output when touched with a finger, and when progressively increasing, weights from 5 to 100 g were placed on it. In Fig. 8, the grasp-and-lift task performed by the robotic hand described in Section II-D is shown. The system starts in `idle` mode from where all the fingers are open. The `catch` command received after 4.5 s triggers the controller to gradually close the fingers until $\overline{\mathbf{F}}_z$ achieves the force threshold for contact of 0.6 N. This process is illustrated in the green patched area of Fig. 8(b) and (c), showing the increasing closure percentage and $\mathbf{F}_z$. At this point, the control loop manages any undesirable in-hand movement, e.g., object slippage. This operation was based on the feedback from $\overline{\mathbf{F}}_{xy}$ [Fig. 8(d)]. In the gray area of Fig. 8(b), the percent closure is pushed to 100% to prevent objects from falling while the human operator fills the beaker with granular material. This behavior was maintained until the `release` mode is triggered by α. In the described experiment, the thumb and the middle finger moved together with the grasped object. F_{xy} remains low in the thumb transducer during this phase. That is an example where the redundancy of fingers is useful in detecting an occasional slippage. Pouring particles into a cup held by flexible appendages exemplifies a chaotic system with inherent uncertainty. The fact that one of the sensors detected the increase in weight is, in fact, a good sign of robustness. The index finger completely counterbalanced the tangential force when the control system increased the hand closure percentage.

In `release` mode, the system perceives an upward force as an intentional attempt to remove the object. Fig. 8(e) and the relative blue area illustrate the hand opening. Further prehensile tasks are shown in Video S2, including grasping a tape, slippery cylinder, and beaker while changing weight.

The choice of a PID controller for the artificial hand is due to its simplicity, and ease of implementation. Indeed, the aim was to show the effectiveness of the proposed optical sensor in achieving stable and reliable performance in grasp-and-lift tasks. Nonetheless, many possible implementations can use more sophisticated control algorithms to handle uncertainty in nonlinear systems [33], [34].

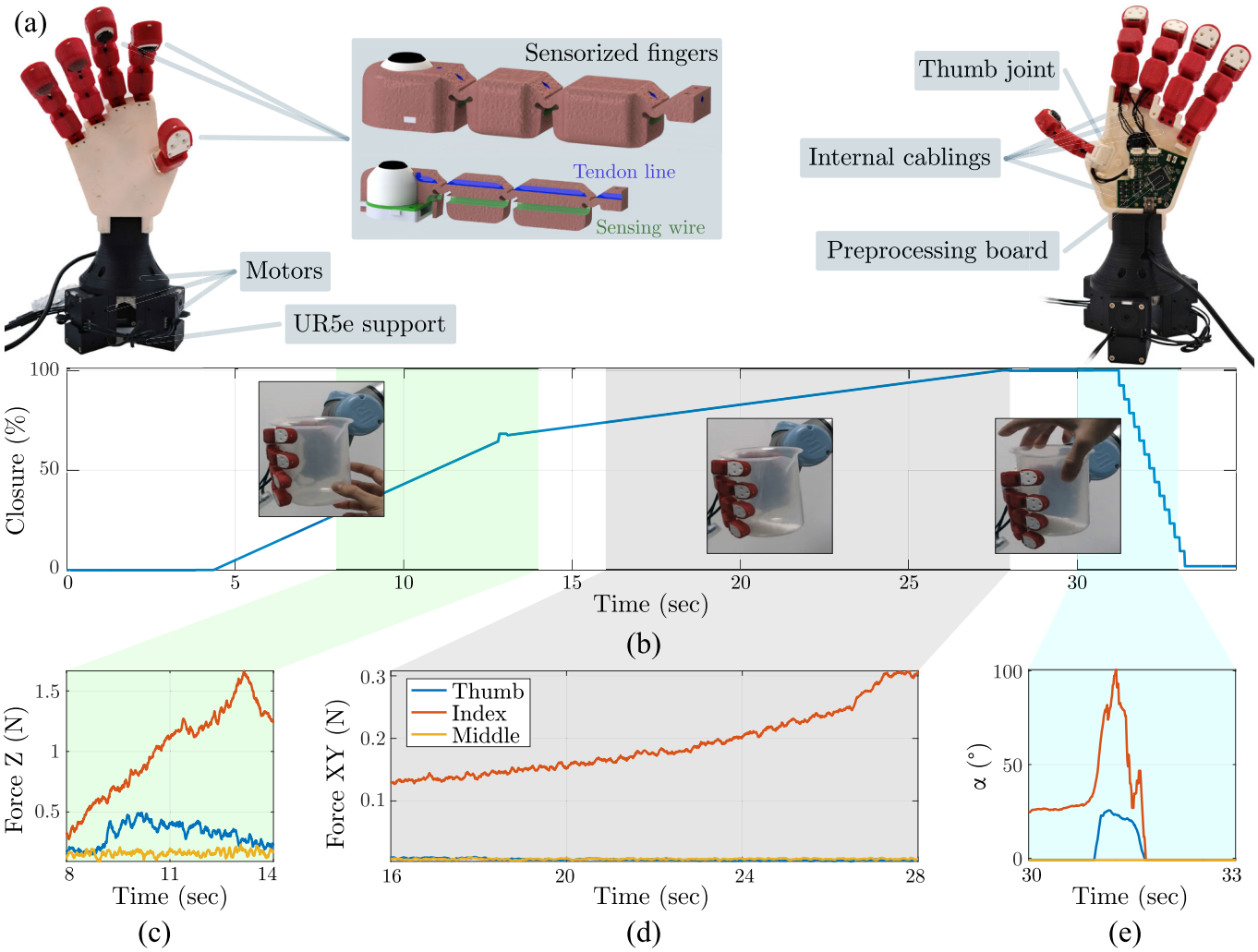

Fig. 8. Custom robotic hand with compliant fingers embedded with the presented sensor. (a) Front and rear views of the sensorized hand with interface to a UR5e arm, internal cabling, hosting structure for the electronics, and thumb joint. The hand adjusts its closure (b) relying on force data to (c) grasp a cup, (d) adapt to a human operator that fills the cup, and (e) release the cup.

IV. Conclusion

Soft optical transducers offer a new avenue for tactile robotics where feedback on the triaxial force is a major requirement. This article introduces a triaxial soft optical force sensor that relies on its 3-D-channeled structure to shape changes in the light path based on an applied force without bulky transduction systems, thus facilitating integration in rigid and deformable substrates. The sensor has cost-effective fabrication procedures and materials, and its size and sensing range can be adjusted to suit specific application requirements. In contrast to FBG-based optical sensors, the 3-D core of the presented solution can be cast to exploit the sensor morphology to convey transduction. The 3-D-channeled prototype showed voltage variations 15 times higher than its bulk analog. An applied force is decomposed into its normal and tangential components of F_{xy} and F_z with an R^2 of 0.93 and 0.98 within a sensing range of 4.05 and 8.50 N, respectively. Furthermore, $\hat{F}_{xy}$ is retrieved using a geometrical transformation from a covariant to Cartesian reference frame. The applications of this solution include artificial hands for feedback control, soft robots with mechanically compatible sensing interfaces, rigid and soft grippers for delicate object handling and manipulation, and continuum arms. Current limitations include the fabrication precision in the scaled-down version and impaired curing process of PDMS in small channels. However, since electronic components are not present in the 3-D architecture, fabrication processes other than casting, e.g., additive manufacturing, can be investigated. Notably, the testing and characterization procedures of uniaxial and triaxial soft sensors lack standardization. Our effort in this direction was to find a decomposition that simplifies force estimation by splitting the process into magnitude and direction estimation. Indeed, a standardized, systematic processing framework could impact the development of new sensors and allow for more effective comparison. Further improvements may arise from optimizing the electronics for different needs, adding custom calibration procedures, and miniaturizing an onboard processing board for single sensor or array.

A plug-and-play system with negligible interferences from external noise, tunable sensing range, scalable size, and small readout electronics like the sensor presented here can be

a game-changing solution wherever triaxial force data are needed.

Author Contributions

Conceptualization: Lucia Beccai, Matteo Lo Preti, and Federico Bernabei; Methodology and Resources: Lucia Beccai and Matteo Lo Preti; Software: Matteo Lo Preti and Anderson B. Nardin; Formal analysis, Data Curation, Visualization, and Writing Original Draft: Matteo Lo Preti; Investigation: Matteo Lo Preti, Federico Bernabei, and Anderson B. Nardin; Writing Review and Editing: Matteo Lo Preti, Federico Bernabei, Anderson B. Nardin, and Lucia Beccai; and Funding Acquisition and Supervision: Lucia Beccai.

Declaration of Interests

The authors declare no competing interests.

Acknowledgment

The authors would like to thank S. Lantean, Soft BioRobotics Perception Laboratory, Istituto Italiano di Tecnologia, for his support in the first stages of the conceptualization and fabrication.

References

[1] Z. Kappassov, J.-A. Corrales, and V. Perdereau, "Tactile sensing in dexterous robot hands—Review," *Robot. Auto. Syst.*, vol. 74, pp. 195–220, Dec. 2015. [Online]. Available: https://linkinghub.elsevier.com/retrieve/pii/S0921889015001621

[2] H. Wang, M. Totaro, and L. Beccai, "Toward perceptive soft robots: Progress and challenges," *Adv. Sci.*, vol. 5, no. 9, p. 1800541, Sep. 2018, doi: 10.1002/advs.201800541.

[3] H. Cho, H. Lee, Y. Kim, and J. Kim, "Design of an optical soft sensor for measuring fingertip force and contact recognition," *Int. J. Control, Autom. Syst.*, vol. 15, no. 1, pp. 16–24, Feb. 2017. [Online]. Available: http://link.springer.com/10.1007/s12555-016-0470-3

[4] P. Yu, L. Chen, P. Zhou, H. Ye, W. Liu, and J. Long, "A compliant three-axis force sensor with solid-liquid hybrid cover for prosthetic fingertip," *IEEE Sensors J.*, vol. 23, no. 16, pp. 18050–18061, Aug. 2023. [Online]. Available: https://ieeexplore.ieee.org/document/10185195/

[5] L. Zhang et al., "Force sensing and feedback system based on novel triaxial force capacitive sensor for minimally invasive surgical robot," *Adv. Sensor Res.*, vol. 2, no. 11, Nov. 2023, Art. no. 2300033, doi: 10.1002/adsr.202300033.

[6] X. Cheng, Y. Gong, Y. Liu, Z. Wu, and X. Hu, "Flexible tactile sensors for dynamic triaxial force measurement based on piezoelectric elastomer," *Smart Mater. Struct.*, vol. 29, no. 7, Jul. 2020, Art. no. 075007. [Online]. Available: https://iopscience.iop.org/article/10.1088/1361-665X/ab8748

[7] Y. Zhu, Y. Liu, Y. Sun, Y. Zhang, and G. Ding, "Recent advances in resistive sensor technology for tactile perception: A review," *IEEE Sensors J.*, vol. 22, no. 16, pp. 15635–15649, Aug. 2022. [Online]. Available: https://ieeexplore.ieee.org/document/9789978/

[8] M. Lo Preti, M. Totaro, E. Falotico, and L. Beccai, "Optical-based technologies for artificial soft tactile sensing," in *Electronic Skin: Sensors and Systems*. Hoboken, NJ, USA: Wiley, 2022, p. 73.

[9] X. Wang, Z. Li, and L. Su, "Soft optical waveguides for biomedical applications, wearable devices, and soft robotics: A review," *Adv. Intell. Syst.*, vol. 6, no. 1, Nov. 2023, Art. no. 2300482, doi: 10.1002/aisy.202300482.

[10] J. Qu et al., "Recent progress in advanced tactile sensing technologies for soft grippers," *Adv. Funct. Mater.*, vol. 33, no. 41, Oct. 2023, Art. no. 2306249, doi: 10.1002/adfm.202306249.

[11] C. Wang et al., "Tactile sensing technology in bionic skin: A review," *Biosensors Bioelectronics*, vol. 220, Jan. 2023, Art. no. 114882. [Online]. Available: https://linkinghub.elsevier.com/retrieve/pii/S0956566322009228

[12] A. Dwivedi, A. Ramakrishnan, A. Reddy, K. Patel, S. Ozel, and C. D. Onal, "Design, modeling, and validation of a soft magnetic 3-D force sensor," *IEEE Sensors J.*, vol. 18, no. 9, pp. 3852–3863, May 2018. [Online]. Available: https://ieeexplore.ieee.org/document/8314107/

[13] T. Kawasetsu, R. Niiyama, and Y. Kuniyoshi, "Flexible and soft inductive tri-axis tactile sensor using liquid metal as sensing target," in *Proc. IEEE SENSORS*. Montreal, QC, Canada: IEEE, Oct. 2019, pp. 1–4. [Online]. Available: https://ieeexplore.ieee.org/document/8956736/

[14] Y. Gong, X. Cheng, Z. Wu, Y. Liu, P. Yu, and X. Hu, "A flexible tactile sensor array for dynamic triaxial force measurement based on aligned piezoresistive nanofibers," *IEEE Sensors J.*, vol. 21, no. 19, pp. 21989–21998, Oct. 2021. [Online]. Available: https://ieeexplore.ieee.org/document/9509515/

[15] A. Gao, Y. Zhou, L. Cao, Z. Wang, and H. Liu, "Fiber Bragg grating-based triaxial force sensor with parallel flexure hinges," *IEEE Trans. Ind. Electron.*, vol. 65, no. 10, pp. 8215–8223, Oct. 2018. [Online]. Available: https://ieeexplore.ieee.org/document/8270709/

[16] T. Li, A. Pan, and H. Ren, "A high-resolution triaxial catheter tip force sensor with miniature flexure and suspended optical fibers," *IEEE Trans. Ind. Electron.*, vol. 67, no. 6, pp. 5101–5111, Jun. 2020. [Online]. Available: https://ieeexplore.ieee.org/document/8766123/

[17] Y. Deng, T. Yang, S. Dai, and G. Song, "A miniature triaxial fiber optic force sensor for flexible ureteroscopy," *IEEE Trans. Biomed. Eng.*, vol. 68, no. 8, pp. 2339–2347, Aug. 2021. [Online]. Available: https://ieeexplore.ieee.org/document/9242290/

[18] D. Cao, J. Hu, Y. Li, S. Wang, and H. Liu, "Polymer-based optical waveguide triaxial tactile sensing for 3-dimensional curved shell," *IEEE Robot. Autom. Lett.*, vol. 7, no. 2, pp. 3443–3450, Apr. 2022. [Online]. Available: https://ieeexplore.ieee.org/document/9695314/

[19] Y. Li, W. Gaozhang, J. Hu, D. Cao, P. Dasgupta, and H. Liu, "Optical-waveguide based 3-axial tactile sensor for minimally invasive surgical instruments," *IEEE Robot. Autom. Lett.*, vol. 9, no. 2, pp. 1604–1611, Feb. 2024. [Online]. Available: https://ieeexplore.ieee.org/document/10373125/

[20] Á. Tar, G. Cserey, and J. Veres, "Sensor device," U.S. Patent 9 513 178, Dec. 6, 2016.

[21] S. Földi, T. Horváth, F. Zieger, P. Sótonyi, and G. Cserey, "A novel non-invasive blood pressure waveform measuring system compared to millar applanation tonometry," *J. Clin. Monitor. Comput.*, vol. 32, no. 4, pp. 717–727, Aug. 2018.

[22] W. Li et al., "L^3 F-TOUCH: A wireless GelSight with decoupled tactile and three-axis force sensing," *IEEE Robot. Autom. Lett.*, vol. 8, no. 8, pp. 5148–5155, Aug. 2023. [Online]. Available: https://ieeexplore.ieee.org/document/10173594/

[23] J. Zhou et al., "Conformable and compact multiaxis tactile sensor for human and robotic grasping via anisotropic waveguides," *Adv. Mater. Technol.*, vol. 7, no. 11, Nov. 2022, Art. no. 2200595.

[24] H. Zheng, Y. Jin, H. Wang, and P. Zhao, "DotView: A low-cost compact tactile sensor for pressure, shear, and torsion estimation," *IEEE Robot. Autom. Lett.*, vol. 8, no. 2, pp. 880–887, Feb. 2023.

[25] J. Ham, A. K. Han, M. R. Cutkosky, and Z. Bao, "UV-laser-machined stretchable multi-modal sensor network for soft robot interaction," *NPJ Flexible Electron.*, vol. 6, no. 1, p. 94, Nov. 2022.

[26] L. Van Duong and V. A. Ho, "Large-scale vision-based tactile sensing for robot links: Design, modeling, and evaluation," *IEEE Trans. Robot.*, vol. 37, no. 2, pp. 390–403, Apr. 2021.

[27] L. Massari et al., "Functional mimicry of Ruffini receptors with fibre Bragg gratings and deep neural networks enables a bio-inspired large-area tactile-sensitive skin," *Nature Mach. Intell.*, vol. 4, no. 5, pp. 425–435, May 2022.

[28] P. S. Gir ao, P. M. P. Ramos, O. Postolache, and J. M. D. Pereira, "Tactile sensors for robotic applications," *Measurement*, vol. 46, no. 3, pp. 1257–1271, Apr. 2013. [Online]. Available: https://linkinghub.elsevier.com/retrieve/pii/S0263224112004368

[29] Z. Wang, A. A. Volinsky, and N. D. Gallant, "Crosslinking effect on polydimethylsiloxane elastic modulus measured by custom-built compression instrument," *J. Appl. Polym. Sci.*, vol. 131, no. 22, Nov. 2014.

[30] S. Lantean, M. Lo Preti, and L. Beccai, "Stretchable reflective coating for soft optical waveguides and sensors," *Soft Matter*, vol. 18, no. 40, pp. 7827–7837, 2022. [Online]. Available: http://xlink.rsc.org/?DOI=D2SM00869F

[31] B. B. Edin, L. Ascari, L. Beccai, S. Roccella, J.-J. Cabibihan, and M. C. Carrozza, "Bio-inspired sensorization of a biomechatronic robot hand for the grasp-and-lift task," *Brain Res. Bull.*, vol. 75, no. 6, pp. 785–795, Apr. 2008.

[32] T. Yoshikai, M. Hayashi, A. Kadowaki, T. Goto, and M. Inaba, "Design and development of a humanoid with soft 3D-deformable sensor flesh and automatic recoverable mechanical overload protection mechanism," in *Proc. IEEE/RSJ Int. Conf. Intell. Robots Syst.*, Oct. 2009, pp. 4977–4983.

[33] V. P. da Fonseca, T. E. A. de Oliveira, and E. M. Petriu, "Estimating the orientation of objects from tactile sensing data using machine learning methods and visual frames of reference," *Sensors*, vol. 19, no. 10, p. 2285, May 2019.

[34] W. Xue, B. Zhou, F. Chen, H. Taghavifar, A. Mohammadzadeh, and E. Ghaderpour, "A constrained fuzzy control for robotic systems," *IEEE Access*, vol. 12, pp. 7298–7309, 2024.

Matteo Lo Preti (Associate Member, IEEE) received the B.Sc. degree in biomedical engineering from the University of Pisa, Pisa, Italy, in 2017, the M.Sc. (cum laude) degree in bionics engineering from the University of Pisa, jointly with Scuola Superiore Sant'Anna, Pisa (MERGE with Sant'Anna School of Advanced Studies), in 2019, and the Ph.D. degree in biorobotics from Scuola Superiore Sant'Anna and the Soft BioRobotics Perception Lab, Genova, Italy, Istituto Italiano di Tecnologia, Genoa, in 2023.

His Ph.D. research focused on soft sensing technologies for tactile-driven intelligent systems. With his multidisciplinary background and keen interest in the intersection of robotics and biology, he strives to contribute to developing innovative solutions in soft sensing and intelligent robotics.

Federico Bernabei (Graduate Student Member, IEEE) received the B.Sc. degree in mechatronic engineering from the University of Modena and Reggio Emilia, Modena, Italy, in 2017, and the M.Sc. degree from the University of Genova, Genoa, Italy, jointly with Jaume I University, Castellón de la Plana, Spain, in 2020. He is currently pursuing the Ph.D. degree in biorobotics with the Sant'Anna School of Advanced Studies (SSSA), Pisa, Italy.

After a brief experience in the hydraulic industry, in 2018, he joined the European Master in Advanced Robotics (EMARO+). His research focuses on soft robotics, particularly soft sensing and soft actuation, with a particular interest in interaction with deformable targets.

Anderson B. Nardin (Student Member, IEEE) received the B.S. degree in electrical engineering with specialization in electronics from the University Center of FEI (FEI), São Bernardo do Campo, Brazil, in 2012, and the M.S. and Ph.D. degrees in space engineering and technology from the National Institute for Space Research (INPE), São Bernardo do Campo, Brazil, in 2015 and 2020, respectively. He is currently pursuing the Ph.D. degree in biorobotics with the Sant'Anna School of Advanced Studies (SSSA), Pisa, Italy.

He is an integral part of the Soft BioRobotics Perception Group. His ongoing research focuses on innovative developments in the field of biorobotics, with a particular emphasis on simulation and the application of robotic technologies.

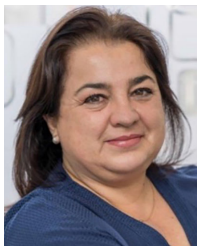

Lucia Beccai (Member, IEEE) received the Electronic Engineering degree from the University of Pisa, Pisa, Italy, and the Ph.D. degree in microsystem engineering from the University of Rome Tor Vergata, Rome, Italy, in 2003.

She is currently a Tenured Senior Researcher with the Istituto Italiano di Tecnologia, Genoa, Italy, leading the Soft BioRobotic Perception Group. With expertise in bioinspired tactile systems and bionics, she holds three patents and has authored over 100 scholarly articles. She actively collaborates on international projects and serves as a Scientific Coordinator for the PROBOSCIS Project. Her research focuses on biorobotics and soft robotics, developing perceptive solutions for safe interactions with humans and the environment.

Open Access funding provided by 'Istituto Italiano di Tecnologia' within the CRUI CARE Agreement